PHYSICAL REVIEW MATERIALS **2**, 094001 (2018)

Two-dimensional superconductivity and topological states in $PdTe_2$ thin films

Chong Liu,[1] Chao-Sheng Lian,[1] Meng-Han Liao,[1] Yang Wang,[1] Yong Zhong,[1] Cui Ding,[1] Wei Li,[1,2] Can-Li Song,[1,2] Ke He,[1,2] Xu-Cun Ma,[1,2] Wenhui Duan,[1,2,3] Ding Zhang,[1,2] Yong Xu,[1,2,4,*] Lili Wang,[1,2,†] and Qi-Kun Xue[1,2,‡]

[1] *State Key Laboratory of Low-Dimensional Quantum Physics, Department of Physics, Tsinghua University, Beijing 100084, People's Republic of China*

[2] *Collaborative Innovation Center of Quantum Matter, Beijing 100084, People's Republic of China*

[3] *Institute for Advanced Study, Tsinghua University, Beijing 100084, People's Republic of China*

[4] *RIKEN Center for Emergent Matter Science (CEMS), Wako, Saitama 351-0198, Japan*

(Received 25 April 2018; revised manuscript received 14 June 2018; published 4 September 2018)

We report on a bottom-up approach via molecular-beam epitaxy to grow high-quality crystalline two-dimensional films of $PdTe_2$ on $SrTiO_3(001)$, and investigation on the electronic and superconducting properties therein by using scanning tunneling microscopy and transport experiments in combination with first-principles calculations. We observed a transition from the narrow-gap semiconducting phase in the monolayer to the metallic phase in the multilayer films. Importantly, all the multilayer films exhibited robust superconductivity, whose transition temperatures in the ultrathin limit were obviously higher than expected from the empirical inverse-of-thickness dependence and could be further enhanced through magnesium intercalation. Our first-principles studies revealed thickness-tuned band topology caused by the significant orbital-dependent interlayer coupling, which explained the experimentally observed thickness-dependent behaviors of atomic and electronic properties. Combined with the prediction of topologically nontrivial states introduced by honeycomb lattice of p orbitals, $PdTe_2$ thin films are promising material candidates for exploring the interplay between superconductivity and topology in the two-dimensional limit.

DOI: 10.1103/PhysRevMaterials.2.094001

I. INTRODUCTION

Two-dimensional (2D) superconductors with truly atomic scale thickness, high crystallinity, and sharp interfaces have attracted intense research interest, which provides great opportunities for exploring interface enhanced high-temperature superconductivity [1–3] and interesting quantum physics like Griffiths singularity [4], quantum metallic phase [5], and Ising superconductivity [6,7]. The discovery of 2D topological materials, like quantum spin Hall [8,9] and quantum anomalous Hall insulators [10], shed light on this field, as the interplay of superconductivity and topology results in emerging physics of topological superconductivity along with exotic elementary excitations of Majorana fermions that are non-Abelian anyons useful for fault-tolerant quantum computation [11–13]. It was proposed that topological superconductivity can be induced in topological boundary states by using superconducting proximity effects [11–13]. However, the effects depend critically on interface conditions, making the experiment quite challenging. Alternatively, a superior proposal is to achieve topological superconductivity by realizing superconductivity and topological electronic states within the same material [14–17]. While many 2D superconductors have been recently discovered [18], very few can simultaneously display topological electronic states [17,19]. In this context, a key experimental object is to fabricate new 2D materials with the coexistence of superconductivity and nontrivial band topology.

Recently, symmetry-protected type-II Dirac semimetals as new states of quantum matter were theoretically proposed and experimentally discovered in transition-metal dichalcogenides (TMDCs) [20–26], like $PtSe_2$, $PtTe_2$, $PdTe_2$, etc. In particular, $PdTe_2$ is an intermetallic compound that becomes superconducting below a critical temperature $T_c = 1.7$ K [25,27,28], making it a promising material candidate to explore the interplay between superconducting quasiparticles and topological Dirac fermions. The $PdTe_2$ bulk has been intensively studied by recent experiments, which a revealed type-II Dirac cone at 0.5 eV below Fermi level [24] together with some possible evidences of conventional type-I superconductivity [28–31]. In contrast, the 2D phase (i.e., thin films of $PdTe_2$), in which more novel phenomena might emerge, remains unexplored.

In this work, we successfully fabricated high-quality $PdTe_2$ thin films with thicknesses varying from monolayer (ML) to 20 MLs on $SrTiO_3(001)$ by using molecular beam epitaxy (MBE), and further investigated the electronic and superconducting properties through *in situ* scanning tunneling microscopy/spectroscopy (STM/STS) and *ex situ* transport measurements in comparison with first-principles calculations. We found that $PdTe_2$ was a narrow-gap semiconductor in the monolayer and transited into a metallic phase at a critical thickness of 2 MLs, implying an unusually strong coupling between van der Waals layers. Importantly, we observed a superconducting transition in films down to 2 MLs and thus discovered a new series of 2D superconductors. We also introduced magnesium intercalation into the thin film

---

[*] Corresponding author: yongxu@mail.tsinghua.edu.cn

[†] Corresponding author: liliwang@mail.tsinghua.edu.cn

[‡] Corresponding author: qkxue@mail.tsinghua.edu.cn

2475-9953/2018/2(9)/094001(8)

and demonstrated an enhancement of T_c. Our first-principles calculations revealed thickness-tuned band topology caused by the significant orbital-dependent interlayer coupling, which explained the thickness-dependent features we observed experimentally. Furthermore, the calculations demonstrated the existence of topologically nontrivial states introduced by honeycomb lattice of p orbitals, suggesting that thin films of $PdTe_2$ (and other similar TMDCs) are candidate materials showing the coexistence of 2D superconductivity and topological states, which hold promise for future research of topological superconductivity and other 2D properties.

II. EXPERIMENTAL AND THEORETICAL METHODS

The Nb-doped $SrTiO_3(001)$ was chosen as substrates. The TiO_2-terminaed surface with in-plane lattice constants of 3.9 Å was obtained after heating to 1100 °C. the $PdTe_2$ films were grown by coevaporating Pd (99.995%) and Te (99.9999%) from Knudsen cells with a flux ratio of 1:2 on $SrTiO_3$ substrate kept at 120 °C. The growth rate is approximately 0.07 ML/min. Mg intercalation was achieved with separate evaporation at 170 °C between the growth intervals of adjacent $PdTe_2$ layers.

A polycrystalline PtIr tip was used throughout the experiments. STM topographic images were acquired in a constant current mode, with the bias voltage (V_s) applied to the sample. Tunneling spectra were measured by disabling the feedback circuit, sweeping the sample voltage V_s, and then extracting the differential conductance dI/dV using a standard lock-in technique with a small bias modulation ($\sim$1% of the sweeping range) at 937 Hz. The transport experiments were performed directly on $PdTe_2$ films. Freshly cut indium cubes were cold pressed onto the sample as contacts. Standard lock-in techniques were employed to determine the sample resistance in a four-terminal configuration with a typical excitation current of 100 nA at 13 Hz. The $V(I)$ characteristics were measured with dc source meters.

First-principles calculations were performed by using density functional theory (DFT) as implemented in the Vienna *ab initio* simulation package [32]. The projector-augmented-wave potential [33], the Perdew-Burke-Ernzerhof (PBE) exchange-correlation functional [34], and the plane-wave basis with an energy cutoff of 350 eV were employed. The Heyd-Scuseria-Ernzerhof (HSE) hybrid functional [35], which is more reliable than PBE in predicting band gaps, was applied to check the band-gap value of monolayer $PdTe_2$. $PdTe_2$ thin films were modeled by the periodic slab approach with a vacuum layer of 15 Å. $24 \times 24 \times 1$ and $24 \times 24 \times 16$ Monkhorst-Pack [36] k-point grids were applied in thin-film and bulk calculations, respectively. The spin-orbit coupling was included in self-consistent electronic structure calculations. The maximally localized Wannier functions were constructed from DFT by the WANNIER90 code [37] and then used to calculate the Wannier charge center [38], the Z_2 topological invariant, and edge states. Lattice dynamics and electron-phonon coupling (EPC) calculations were performed by using density functional perturbation theory [39] as implemented in the Quantum ESPRESSO package [40], which employed the ultrasoft pseudopotential, the plane-wave basis with an energy cutoff of 40 Ry, and a sampling of electronic (vibrational) Brillouin zones by $32 \times 32 \times 1$ ($8 \times 8 \times 1$) meshes. The superconducting transition temperature was evaluated by using the Allen-Dynes modified McMillan formula [41] with a typical Coulomb pseudopotential $\mu^* = 0.1$.

III. EXPERIMENTAL RESULTS

The bulk $PdTe_2$ has a $1T$-CdI_2 type layered crystal structure with the $P\bar{3}m1$ space group [42]. It is composed of inversion symmetric Te-Pd-Te layers that show *AA* stacking along the (0001) direction [Fig. 1(a)]. The in-plane and out-of-plane lattice constants are $a = 4.04$ Å and $c = 5.13$ Å, respectively [42]. Despite lattice mismatch with the tetragonal $SrTiO_3(001)$ surface, we successfully grew atomically flat crystalline $PdTe_2(0001)$ thin films using MBE, as consistently evidenced by x-ray-diffraction and STM measurements. As shown in Fig. 1(b), a normal ω-2θ scan curve of 10-ML films displays three peaks from $PdTe_2$ (0001), (0002), and (0003) and two peaks from $SrTiO_3(001)$ and (002). Displayed in Fig. 1(d) [Fig. 1(e)] is the STM topographic image of $PdTe_2$ films with nominal coverages of 1.1 MLs (2.3 MLs) showing uniform atomically flat films with some additional $PdTe_2$ patches. The bright line-shaped features in Fig. 1(e) correspond to domain walls, around which the lattice is rotated by 15° [Fig. 1(f)].

The lattice mismatch between $PdTe_2(0001)$ and $SrTiO_3(001)$ could lead to thickness-dependent lattice constants of $PdTe_2$ films. Indeed, x-ray-diffraction results demonstrated thickness-tuned out-of-plane lattice constants. As shown in Fig. 1(c), the $PdTe_2$ (0001) peak is centered at 17.107° for 10-ML films and 17.221° for 20-ML films, compared to 17.477° for bulk $PdTe_2$ (JCPDS card number: 29–0970). The corresponding calculations give an out-of-plane lattice expansion of 2.1% for 10 MLs and 1.5% for 20 MLs compared to the bulk value. On the other hand, the atomically resolved STM topography images give consistent in-plane lattice constants within experimental uncertainty, despite film thickness. Displayed in Figs. 2(a)–2(d) are the atomically resolved topography images of 2- and 15-ML films and the corresponding fast Fourier transform (FFT) images, which consistently indicate hexagonal lattices with in-plane lattice constant of 4.0 ± 0.1 Å. We speculate that the in-plane lattice constant variation could be within the lateral resolution of STM, therefore it is unresolvable.

It is worth noting that signature of stripe charge order emerged in ultrathin films and decayed with increasing film thickness. As displayed in Fig. 2(a), the atomically resolved image of 2-ML films taken at 100 meV shows stripe order along the $[1\bar{1}00]$ direction with a period of $\sim$7 Å. The stripe order is further identified from the corresponding FFT image inserted in Fig. 2(a), which shows a pair of spots marked by yellow circles in addition to the 1×1 Bragg points. In contrast, the topographic image taken at -100 meV and the corresponding FFT image show the same hexagonal lattice structure without signature of stripe order [Fig. 2(b)]. In the case of 15 MLs, the features of stripe order are only discernable from the FFT image but not directly on the topography image [Fig. 2(c)]. The stripe order, which is bias and thickness dependent and directed along the high-symmetry direction of the $PdTe_2$ lattice, bears resemblance to the charge density wave in other TMDC materials [43], rather than the sample-bias insensitive Moiré pattern.

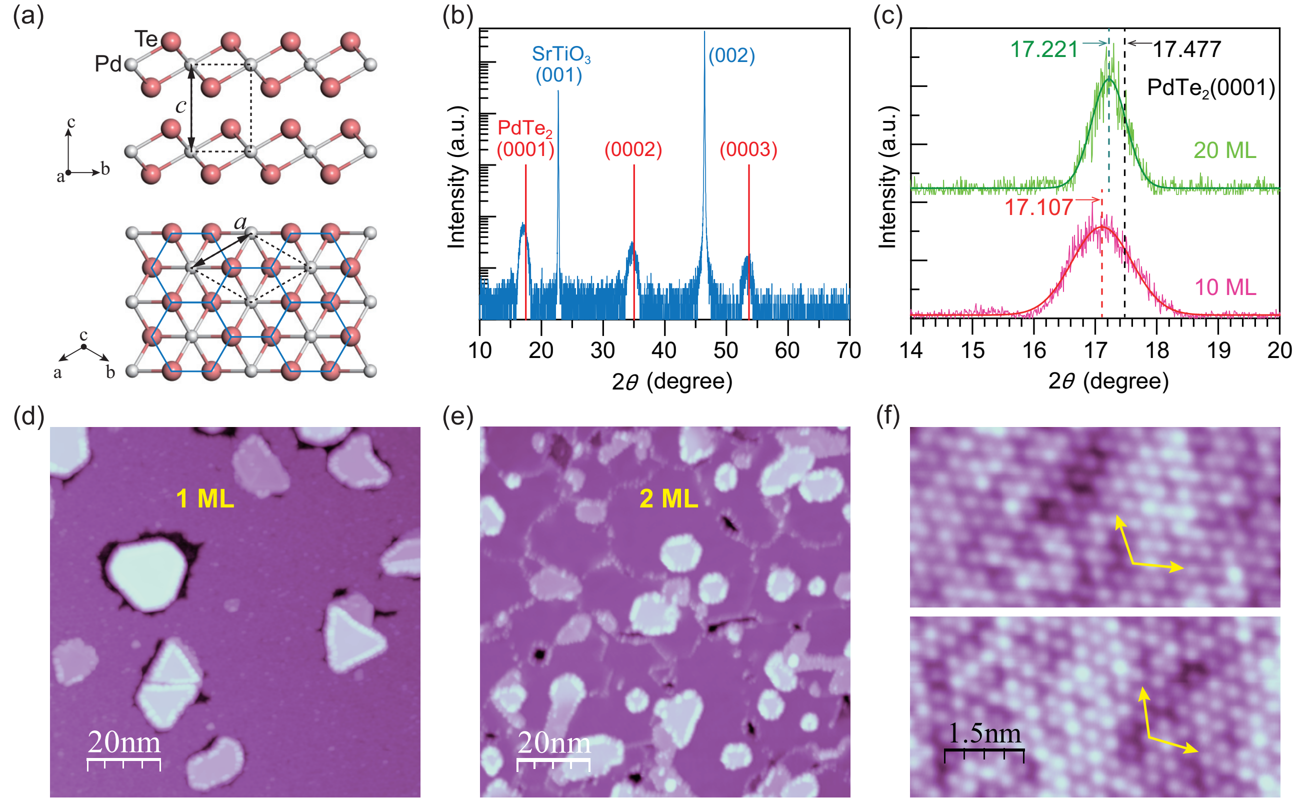

FIG. 1. Structure and morphology of $PdTe_2$ films on $SrTiO_3(001)$. (a) Lattice structure schematic of $PdTe_2$. A buckled honeycomb lattice is formed by Te atoms, as denoted by blue lines. (b) X-ray-diffraction pattern of 10-ML $PdTe_2$ films on $SrTiO_3(001)$ substrate. (c) The (0001) XRD peaks of 10 and 20-ML $PdTe_2$ films. The solid lines are the Gaussian fits and the extracted peak positions are marked by dashed lines. The black dashed line marks the (0001) peak position of bulk $PdTe_2$. (d),(e) STM topographic images of $PdTe_2$ films with nominal coverage of 1.1 MLs ($V_s = 2\,\mathrm{V}$, $I = 50\,\mathrm{pA}$) and 2.3 MLs ($V_s = 2\,\mathrm{V}$, $I = 40\,\mathrm{pA}$), respectively. (f) Topographic images taken on adjacent domains ($V_s = 50\,\mathrm{mV}$, $I = 500\,\mathrm{pA}$) of 4-ML films. The yellow arrows indicate the lattice orientations.

Differential tunneling conductance (dI/dV) spectra, where the density of states (DOS) around the Fermi level were measured, show a transition from the narrow-gap semiconducting phase in the monolayer to the metallic phase in the multilayers. Figure 2(e) summarizes the typical tunneling spectra of 1-, 2-, 3-, and 15-ML films taken at 4.8 K. For monolayer $PdTe_2$, the tunneling conductance was close to zero around the Fermi level and rose up quickly with increasing energy, indicative of a narrow-gap semiconducting behavior. In contrast, all multilayer films showed much higher tunneling conductance with peaks near the Fermi level, indicating a metallic nature. This significant band-structure evolution can be interpreted as a result of interlayer p_z orbital coupling, as shown later.

To investigate the superconductivity and its evolution with thickness, we performed systematic *ex situ* transport measurements directly on $PdTe_2$ films with thickness d between 2.5 and 20 MLs. Figures 3(a) and 3(b) summarize the resistance as a function of temperature for 2.5-, 4-, 10-, and 20-ML films, normalized by the resistance at 273 and 3 K, respectively. Clearly, sharp resistance drops occurred and moved to higher temperature with increasing thickness, and zero resistance was reached for films thicker than 4 MLs [Fig. 3(b)]. We defined T_c as the temperature where the resistance drops to half of that of the normal state and showed its relationship with inverse of film thickness d in Fig. 3(f). T_c increased from 0.30 K for 2.5-ML films to 0.68 K for 4-ML films and then continued increasing gradually. Drawing a line between the points of 10 and 20 MLs and then extrapolating to infinite thickness yielded a T_c of 1.8 K, which agrees well with the bulk T_c of $PdTe_2$ samples [25,27,28]. This suggests that the T_c of films thicker than 10 ML scales linearly with $1/d$, following the empirical formula

$$T_c(d) = T_{c0}(1 - d_c/d), \tag{1}$$

where T_{c0} is the critical temperature of the bulk, and d_c is the thickness threshold for the superconductivity. This empirical phenomenon can be explained by adding a surface-energy term in the Ginzburg-Landau free energy of a superconductor [44], since the surface-to-volume ratio is dominant in thin films.

According to Eq. (1), the d_c here was estimated to be 4 MLs, suggesting that films thinner than 4 MLs should not be superconducting. In reality, both 4- and 2.5-ML films exhibited superconducting transitions. Considering the contrast of local density of states around Fermi level between 1-ML films and multilayer films revealed by STS [Fig. 2(e)], we suspect that the charge transfer from the substrate, if it exists, might play a minor role here, since it should have been stronger in monolayer films than in multilayers [2,3]. Instead, the robust superconductivity in the thinner films could be due to intrinsic two-dimensional electronic properties or strain effect due to lattice mismatch with the $SrTiO_3$ substrate. Moreover, the superconductivity was further enhanced with Mg intercalation, which could be originated from electron doping as in the

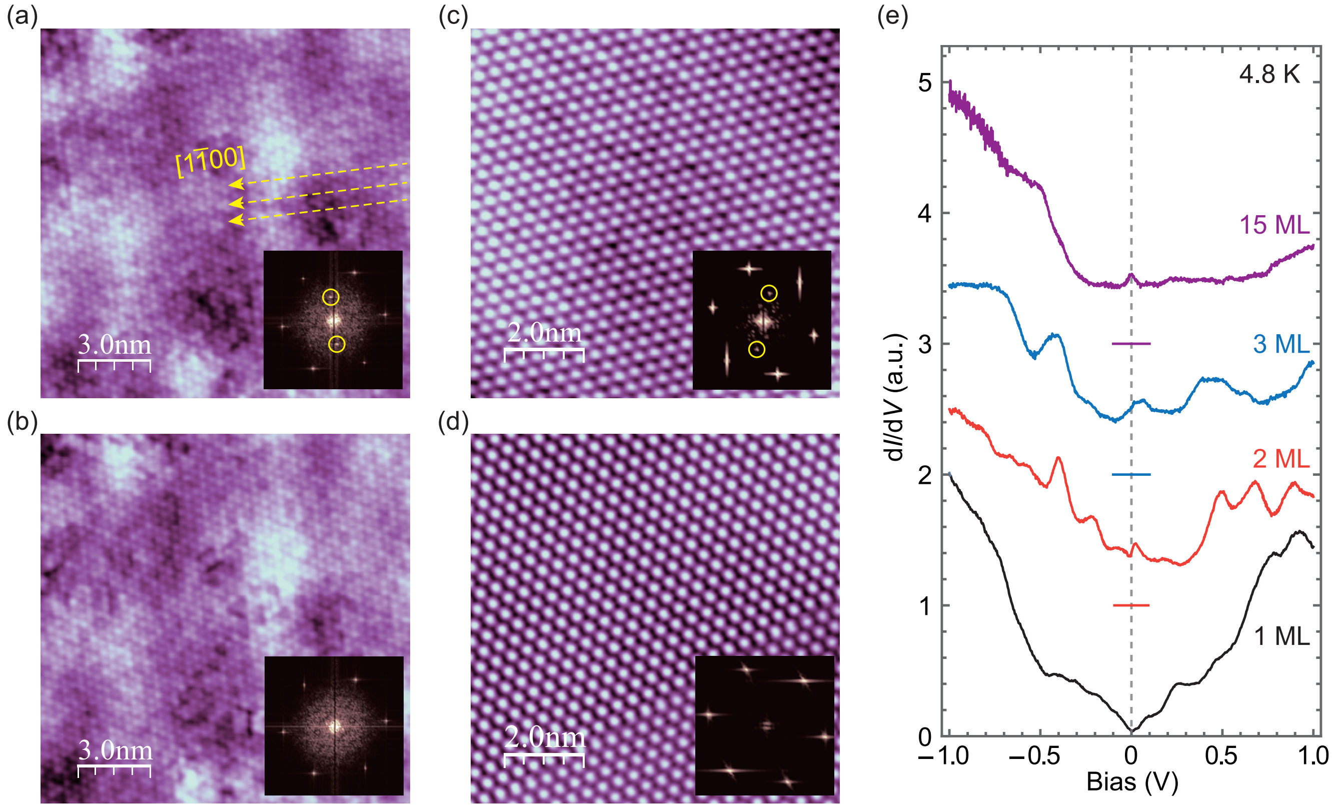

FIG. 2. Electronic characteristics of $PdTe_2$ films on $SrTiO_3(001)$. (a),(b) and (c),(d) Topographic images taken on 2-ML films [(a) $V_s = 100\,mV$, $I = 2\,nA$; (b) $V_s = -100\,mV$, $I = 2\,nA$] and 15-ML films [(c) $V_s = 100\,mV$, $I = 140\,pA$; (d) $V_s = 200\,mV$, $I = 140\,pA$], respectively, with the insets representing the corresponding FFT images. The yellow dashed arrows and circles in (a) and (c) mark the features from stripe order. (e) Typical tunneling spectra taken on $PdTe_2$ films at 4.8 K: 1 ML ($V_s = 1\,V$, $I = 500\,pA$), 2 MLs ($V_s = 1.5\,V$, $I = 500\,pA$), 3 MLs ($V_s = 1.5\,V$, $I = 500\,pA$), and 15 MLs ($V_s = 1.5\,V$, $I = 600\,pA$). The spectra are shifted along the vertical axis. The horizontal bars with the same color mark the zero conductance for each curve.

case of copper intercalated $PdTe_2$ [45] or interlayer coupling modulation as molecule-intercalated TaS_2 [46]. As shown in Fig. 3(b), T_c increased to 1.0 K and zero resistance was reached at 0.9 K after Mg intercalation for 4-ML $PdTe_2$ films.

The temperature dependence of resistance in a normal state nicely illustrated the evolution from insulatinglike to metallic behavior as d was increased from 2.5 to 20 MLs [Fig. 3(a)]. The parabola fittings for 10- and 20-ML films prior to the onset of superconductivity, marked by light green curves, indicated Fermi-liquid behavior. The 10- and 20-ML films showed standard metallic behavior and the 2.5-ML films were found to be insulatinglike, and the 4-ML films straddled the boundary between the insulatinglike and metallic states. Both domain walls and surface adsorption (during the short period when the samples were in ambient environment being prepared for transport measurements) can induce disorder and electron localization and then facilitate insulatinglike transport behaviors in ultrathin films. However, robust superconducting transitions were clearly demonstrated by such macroscopic transport measurements for all multilayer films, which makes $PdTe_2$ a good platform for investigating 2D properties.

Besides T_c, the upper critical filed H_{c2} was also thickness tuned. We measured the resistance as a function of temperature in various perpendicular magnetic fields for 4-, 10-, and 20-ML $PdTe_2$ films [see Supplemental Material Figs. S1(a)–S1(c) [47]], applied a criterion of 50% normal resistance recovery to the $R(T, H)$ curves to define the upper critical field $H_{c2}(T)$, and displayed its relation with normalized temperature T/T_c in Fig. 3(c). Fittings based on the Ginzburg-Landau formula [48]

$$\mu_0 H_{c2}(T) = \frac{\Phi_0}{2\pi\xi^2}\left(1 - \frac{T}{T_c}\right) \qquad (2)$$

and a two-band model [47,49] are displayed as dashed and solid lines, respectively. In Eq. (2), $\mu_0 H_{c2}$ is the upper critical field, ξ is the in-plane coherent length at zero temperature, $\Phi_0 = h/2e$ is the flux quantum, and T_c is the superconducting transition temperature at zero field. The H_{c2}-T relation agrees better with the two-band model than the Ginzburg-Landau formula, in particular for 4-ML films [Fig. 3(c)]. As summarized in Fig. 3(f), the two fittings gave $H_{c2}(0)$ values with a small discrepancy. They are $H_{c2,\,4\,ML}(0) \approx 0.50\,T\,(0.52\,T)$, $H_{c2,\,10\,ML}(0) \approx 0.17\,T\,(0.13\,T)$, and $H_{c2,\,20\,ML}(0) \approx 0.10\,T\,(0.08\,T)$ from the Ginzburg-Landau fitting (two-band model fitting). In contrast to the decrease of T_c with decreasing thickness, the H_{c2} was strongly enhanced in thinner films. We further derived the in-plane coherent length ξ from Eq. (2) with $H_{c2}(0)$ deduced from linear fitting, and obtained $\xi_{4\,ML} \approx 26\,nm$, $\xi_{10\,ML} \approx 44\,nm$, and $\xi_{20\,ML} \approx 57\,nm$. These thickness-dependent results agree with Pippard's theory: the effective

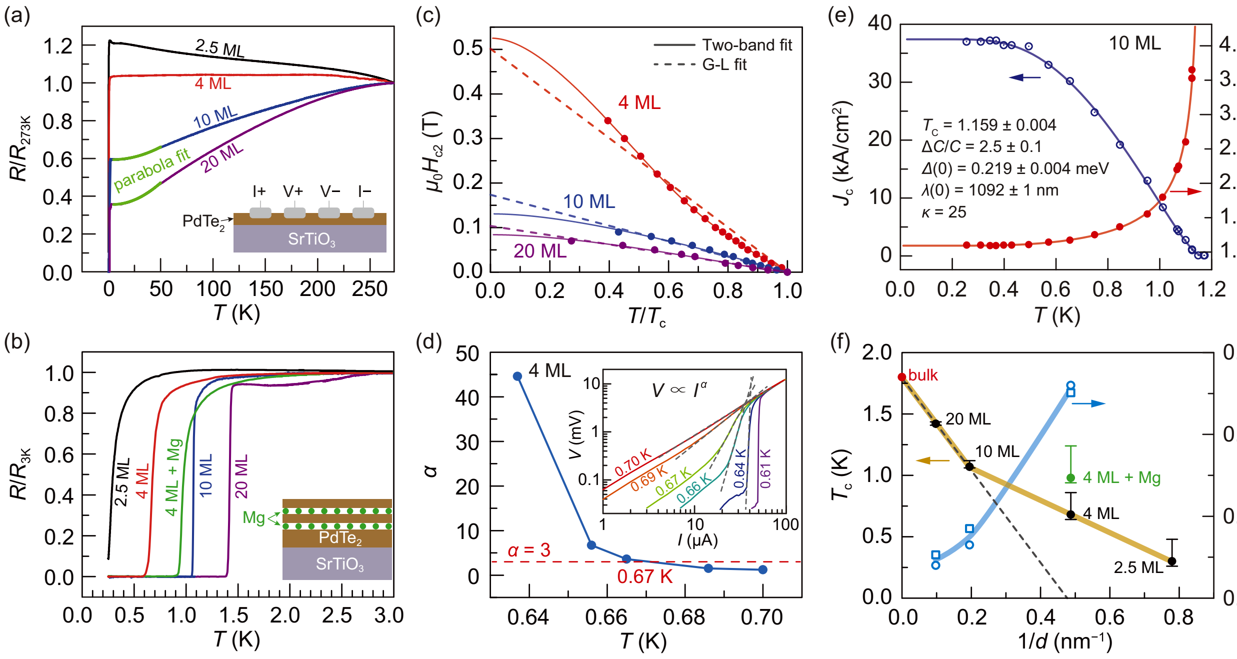

FIG. 3. Transport characterization of PdTe$_2$ films on SrTiO$_3$(001). (a),(b) Temperature dependence of the resistance of PdTe$_2$ films with various thickness. The insets of (a) and (b) are schematic for four-probe transport measurements and the sketch of 4-ML Mg$_x$PdTe$_2$, respectively. (c) Out-of-plane upper critical field vs normalized temperature T/T_c plot fitted with the linear Ginzburg-Landau (GL) formula (dashed lines) and two-band model (solid lines). (d) The variation of exponent α as a function of temperature, extracting from the inset power-law fittings (gray dashed lines) in V-I characteristics, for 4-ML films. (e) Temperature dependence of J_c (blue dots) and λ (red dots) derived from Eq. (3) for 10-ML films. The solid curves are the BCS fittings. (f) T_c and $H_{c2}(T = 0)$ evolution as a function of the inverse of film thickness. The squares and circles represent the $H_{c2}(0)$ derived from the GL formula and two-band model, respectively.

coherent length ξ decreases with decreasing mean free path [50]. The latter decreases with thickness, most likely resulting from stronger disorder in thinner films as indicated by the normal-state R-T behaviors shown in Fig. 3(a).

The V-I characteristics demonstrated signatures of Berezinski-Kosterlitz-Thouless (BKT) transition and type-II superconductivity, which verifies the 2D superconductivity nature of PdTe$_2$ thin films. We exemplified the V-I characteristics for 4 MLs and the derived J_c-T relation for 10-ML films in Figs. 3(d) and 3(e), respectively. As clearly shown in the inset of Fig. 3(d), the V-I characteristics exhibit a power-law dependence: $V \propto I^\alpha$. A detailed evolution of the exponent α as a function of temperature is summarized in the main panel of Fig. 3(d). The exponent α increased systematically with decreasing temperature as expected for the BKT transition and approached 3 at 0.67 K, which was identified as $T_{\rm BKT}$ [51]. The $T_{\rm BKT}$ value agrees well with the $T_c = 0.68$ K deduced from the R - T curve. As demonstrated by the derived J_c - T relation for 10 MLs in Fig. 3(e) [47], with decreasing temperature, J_c increased and got saturated to $J_c(0) \approx 37\,\text{kA/cm}^2$. Assuming type-II superconductivity as normally occurs in thin films, J_c correlates with the London penetration depth λ and the Ginsburg-Landau parameter $\kappa = \lambda/\xi$:

$$J_c(T) = \frac{\Phi_0}{4\pi\mu_0}\frac{\ln(\kappa) + 0.5}{\lambda^3(T)}, \tag{3}$$

where μ_0 is the magnetic permeability of free space [52]. By adopting $\xi = 44$ nm, we derived $\lambda(0) \approx 1.1\,\mu$m and $\kappa \approx 25 \gg 1/\sqrt{2}$, agreeing with the assumption of type-II superconductivity. Furthermore, the $J_c(T)$ and $\lambda(T)$ could be nicely fitted with BSC expressions for $\lambda(T)$ and superconducting gap $\Delta(T)$ [47,52], and $\Delta(0)$ was estimated to be 0.22 meV [Fig. 3(e)]. It is worth noting that the calculation with the formula assumed for type-I superconductors also gave $\kappa \gg 1/\sqrt{2}$, in contradiction to the assumption [47]. Thus, our results indicate a transition to type-II thin-film superconductivity from type-I bulk superconductivity. The critical thickness for such transition is beyond 10 MLs.

IV. CALCULATION RESULTS AND DISCUSSION

We performed first-principles density functional theory (DFT) calculations to pursue a comprehensive understanding on the atomic, electronic, topological, and superconducting properties of PdTe$_2$ thin films. PdTe$_2$ is characterized by distinct orbital occupations that d orbitals of the transition metal Pd are fully occupied while p orbitals of the chalcogen Te are partially unoccupied [see the orbital projection in Fig. 4(a)]. The key orbital feature results in two important material properties: (i) Based on the chemically inert nature of Pd, each monolayer of PdTe$_2$ can be effectively viewed as a buckled honeycomb structure of Te [Fig. 1(a)]. Thus a honeycomb lattice of p orbitals is realized by this material, which is intriguing for exploring topological quantum effects [53]. (ii) Due to the chemically active nature of Te, coupling between van der Waals layers could be unusually strong in PdTe$_2$. The interlayer coupling is relatively strong (weak) between out-of-plane p_z orbitals (in-plane p_{xy} orbitals) of Te, leading to significant orbital-dependent quantum effects. These

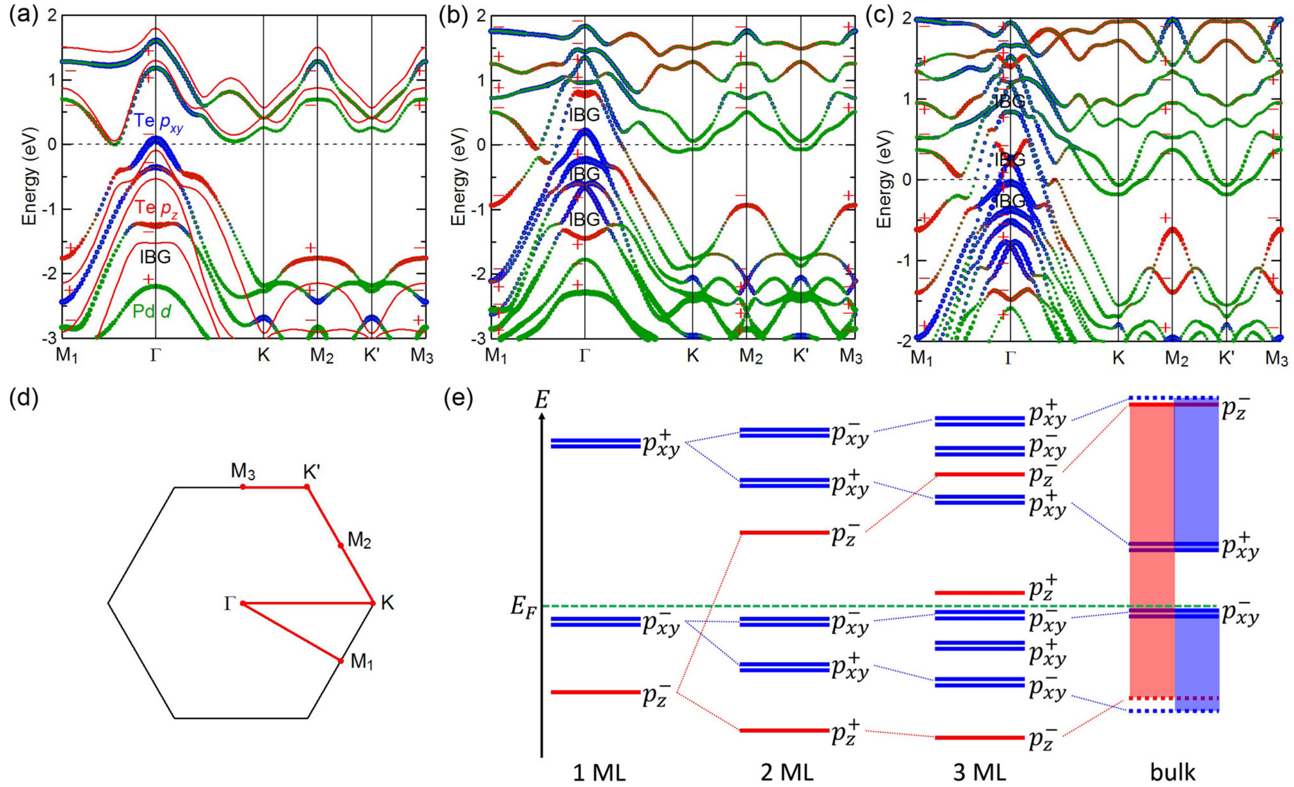

FIG. 4. DFT calculated electronic and topological properties of $PdTe_2$ thin films. (a)–(c) DFT-PBE calculated band structures for $PdTe_2$ thin films of 1-, 2-, and 3-ML $PdTe_2$ thin films, respectively, along the high-symmetry lines of Brillouin zone depicted in (d). Blue, red, and green colors highlight the contributions from Te p_{xy}, Te p_z and Pd d orbitals, respectively. "+, −" labels at the time-reversal invariant points (Γ, $M_{1,2,3}$) denote parities of Bloch wave functions. "IBG" represents inverted band gap with nontrivial topological invariant $Z_2 = 1$, which is well defined when the direct band gap is nonzero at every $\boldsymbol{k}$ point. DFT-HSE calculated band structure is shown by red solid lines in (a). (e) Schematic diagram showing the evolution of p_{xy} (blue) and p_z (red) levels of Te at the Γ point from 1, 2, 3 MLs to bulk $PdTe_2$, in which the SOC effect is excluded. The bonding p_z level of 1 ML is far below the Fermi level and thus not shown. Parities of Bloch wave functions are given as superscripts. For the bulk, band broadening of p_{xy} and p_z orbitals along the Γ-A direction is represented by blue and red shades, respectively.

essential characteristics form the basis for understanding the thickness-dependent behaviors of $PdTe_2$ thin films.

Atomic structures of $PdTe_2$ thin films displayed observable thickness dependence. The calculated in-plane lattice constant of $PdTe_2$ was $a = 4.028$ Å for 1 ML and $a = 4.097$ Å for bulk, showing a monotonic increase with increasing film thickness. An opposite trend was found for the averaged out-of-plane lattice constant, which decreased from $c = 5.263$ Å for 2 MLs to $c = 5.190$ Å for bulk (see Supplemental Material Table S1 [47]). The predicted lattice constants agree well with the experimental values ($a = 4.04$ Å and $c = 5.13$ Å for bulk), considering that DFT-PBE typically overestimates lattice constants slightly. Moreover, the thickness-dependent feature is consistent with our x-ray-diffraction measurements. Intuitively, the intralayer and interlayer Te-Te couplings compete with each other. As the film thickness increases, the strength of intralayer (interlayer) Te-Te coupling gradually reduces (enhances), leading to an expansion (contraction) of a (c). Thus the interplay between intralayer and interlayer Te-Te couplings explains the variance of lattice constants with film thickness.

Profound thickness dependence of electronic band structures was found in $PdTe_2$ thin films. Bulk $PdTe_2$ is well established to be a metal (having type-II topological Dirac points ∼0.5 eV below the Fermi level) [23,24]. In contrast, $PdTe_2$ in the monolayer limit was predicted to be a narrow-gap semiconductor (indirect gap ∼0.14 eV) by the advanced hybrid functional method [Fig. 4(a)], while DFT-PBE, which typically underestimates band gap due to the self-interaction error, predicted a semimetal phase with minor overlap between valence and conduction bands [Fig. 4(a)]. The narrow-gap feature of monolayer $PdTe_2$ is consistent with our STS measurements [Fig. 2(e)]. The evolution of band structure with varying film thickness is visualized in Figs. 4(a)–4(c). In bilayer $PdTe_2$, the interlayer coupling induces significant band splitting, whose strength is moderate for p_{xy}-orbital bands and considerably strong for p_z-orbital bands. As a result, the p_z-orbital valence bands are pushed far above the Fermi level, leading to metallic states. Thicker films also give metallic states as in the bulk. Thus, a semiconductor-to-metal transition happened at the very thin thickness of 2 MLs, as observed by STS [Fig. 2(e)], which was driven by the strong interlayer coupling between p_z orbitals.

Moreover, we theoretically investigated superconducting properties of $PdTe_2$ by using a modified McMillan formula [41,54] within the framework of Bardeen-Cooper-Schrieffer (BCS) theory. For bulk $PdTe_2$, the predicted T_c of 1.78 K agrees well with the experimental value of 1.7 K (see Supplemental Material Table S2 [47]). This good agreement suggests that bulk $PdTe_2$ is a BCS superconductor, as confirmed by recent experiments [28,29,31]. For $PdTe_2$ thin films, the predicted T_c are 1.42, 1.52, and 0.97 K for 2, 3, and 4 MLs, respectively, which are higher than the experimental values but display a suppression of T_c compared to the bulk value as found experimentally. Moreover, distinct from experiment, theoretical T_c showed a nonmonotonic thickness dependence, mainly ascribed to the thickness-dependent DOS at the Fermi level (included by the electron-phonon coupling parameter presented in Table S2 [47]). These discrepancies might be caused by the neglect of interface and disorder effects in theory, or more intriguingly imply the emergence of an unconventional superconducting phase in $PdTe_2$ thin films.

To illustrate effects of the spin-orbit coupling (SOC) and interlayer coupling, we presented the band structure without the SOC [see Supplemental Material Figs. S2(a)–S2(c) [47]] and a schematic diagram of band splitting induced by interlayer coupling [Fig. 4(e)]. Hereafter, electronic states at the Γ point are discussed if not explicitly mentioned. In monolayer $PdTe_2$, the crystal field induced a band splitting between p_{xy} and p_z orbitals of Te, locating p_z below p_{xy}. Moreover, these orbitals respectively formed bonding and antibonding states by the intralayer Te-Te coupling, with the antibonding p_z located below the bonding p_{xy}. The SOC generated a sizable band splitting of ∼0.4 eV for p_{xy} at the Γ point, caused by the heavy atomic mass of Te. An inverted band gap (IBG) existed just below the p_z-orbital band [Fig. 4(a)]. This is rationalized by the fact that the material hosts a (buckled) honeycomb lattice of p orbitals, thus showing nontrivial Z_2 band topology as in other graphenelike materials [55,56]. In the bilayer, the interlayer coupling induced band splitting (excluding the SOC) was 0.4–0.5 eV for p_{xy} but much larger for p_z (∼1.8 eV), which pushed the upper p_z-orbital band higher than some lower p_{xy}-orbital bands [Fig. 4(e)]. Topological band inversions thus happened between p_z-orbital and p_{xy}-orbital bands of opposite parities, generating three IBGs near the Fermi level [Fig. 4(b)]. As the film thickness increased, the upper p_z-orbital band moved further upwards and finally became higher than most p_{xy}-orbital bands in the bulk limit [Fig. 4(e)], leading to topological phase transitions and the appearance/disappearance of IBGs. The nontrivial band topology is further confirmed by calculating Wannier charge centers (data not shown) [38]. Furthermore, we computed edge states of thin films and found some edge modes [see Supplemental Material Figs. S2(d)–S2(f) [47]]. However, it is difficult to distinguish their topological nature as the edge states always significantly overlap with the bulk states. This also explains our STS results that showed no clear signature of edge states (see Supplemental Material Fig. S3 [47]). Further low-temperature experiments are needed to prove the existence of 2D IBGs in $PdTe_2$ thin films.

V. CONCLUSIONS

To summarize, the $PdTe_2$ films with thicknesses between 1 and 20 MLs exhibited thickness-dependent atomic, electronic, and superconducting properties, as experimentally presented by various lattice constant, DOS, T_c, and H_{c2}, which can be basically attributed to competition between interlayer and intralayer coupling in the 2D form. All multilayer films showed robust superconductivity, and the ultrathin ones exhibited charge order phase as well. The robust 2D superconductivity observed experimentally, together with the existence of topologically nontrivial states in $PdTe_2$ thin films introduced by honeycomb lattice of p orbitals as our first-principles calculations revealed, suggests that ultrathin films of $PdTe_2$ are promising material candidates for exploring topological superconductivity and interesting 2D properties. Further transport studies under low temperatures and spectroscopy investigations in momentum space on such ultrathin films are expected to unveil exotic properties including interplay between superconductivity and topological states in the 2D limit.

Finally, we would like to comment on the possible implication from viewpoints of sample preparation and interface engineering. We provided a bottom-up approach via molecular beam epitaxial technique and realized the controllable van der Waals epitaxial growth of compact 2D atomic crystalline films of $PdTe_2$ on $SrTiO_3(001)$. This bottom-up approach most likely works for other type-II symmetry-protected topological Dirac semimetals, like $PtSe_2$, $PtTe_2$, $PdSe_2$, etc., where topological states and superconductivity may coexist. Furthermore, such epitaxial growth provides additional modulation on the lattice structure by substrate strain (resembling high pressure condition), introduces interface charge doping, and hence enables manipulating on superconductivity [14], topological states [23], charge density wave [57], and hybridization between them [14]. The synthetic interface effects might induce enhanced T_c and create emerging quantum phenomena.

ACKNOWLEDGMENTS

The work was supported by NSFC (Grants No. 11574174, No. 11774193, No. 11790311, No. 11674188, and No. 11334006) and MOST of China (Grants No. 2015CB921000, No. 2017YFA0303303, No. 2016YFA0301001, and No. 2018YFA0305603). Y.X. acknowledges support from Tsinghua University Initiative Scientific Research Program and the National Thousand-Young-Talents Program. The calculations were done on the "Explorer 100" cluster system of Tsinghua University and on the "Tianhe-2" of National Supercomputer Computer Center in Guangzhou.

---

[1] T. Zhang, P. Cheng, W.-J. Li, Y.-J. Sun, G. Wang, X.-G. Zhu, K. He, L.-L. Wang, X. Ma, X. Chen, Y. Wang, Y. Liu, H.-Q. Lin, J.-F. Jia, and Q.-K. Xue, Nat. Phys. **6**, 104 (2010).

[2] Q.-Y. Wang, Z. Li, W.-H. Zhang, Z.-C. Zhang, J.-S. Zhang, W. Li, H. Ding, Y.-B. Ou, P. Deng, K. Chang, J. Wen, C.-L. Song, K. He, J.-F. Jia, S.-H. Ji, Y.-Y. Wang, L.-L. Wang, X. Chen, X.-C. Ma, and Q.-K. Xue, Chin. Phys. Lett. **29**, 037402 (2012).

[3] L. Wang, X. Ma, and Q.-K. Xue, Supercond. Sci. Technol. **29**, 123001 (2016).

[4] Y. Xing, H.-M. Zhang, H.-L. Fu, H. Liu, Y. Sun, J.-P. Peng, F. Wang, X. Lin, X.-C. Ma, Q.-K. Xue, J. Wang, and X. C. Xie, Science **350**, 542 (2015).

[5] A. W. Tsen, B. Hunt, Y. D. Kim, Z. J. Yuan, S. Jia, R. J. Cava, J. Hone, P. Kim, C. R. Dean, and A. N. Pasupathy, Nat. Phys. **12**, 208 (2015).

[6] J. M. Lu, O. Zheliuk, I. Leermakers, N. F. Q. Yuan, U. Zeitler, K. T. Law, and J. T. Ye, Science **350**, 1353 (2015).
[7] X. Xi, Z. Wang, W. Zhao, J.-H. Park, K. T. Law, H. Berger, L. Forró, J. Shan, and K. F. Mak, Nat. Phys. **12**, 139 (2015).
[8] B. A. Bernevig, T. L. Hughes, and S.-C. Zhang, Science **314**, 1757 (2006).
[9] M. König, S. Wiedmann, C. Brüne, A. Roth, H. Buhmann, L. W. Molenkamp, X.-L. Qi, and S.-C. Zhang, Science **318**, 766 (2007).
[10] C.-Z. Chang, J. Zhang, X. Feng, J. Shen, Z. Zhang, M. Guo, K. Li, Y. Ou, P. Wei, L.-L. Wang, Z.-Q. Ji, Y. Feng, S. Ji, X. Chen, J. Jia, X. Dai, Z. Fang, S.-C. Zhang, K. He, Y. Wang, L. Lu, X.-C. Ma, and Q.-K. Xue, Science **340**, 167 (2013).
[11] L. Fu and C. L. Kane, Phys. Rev. Lett. **100**, 096407 (2008).
[12] M. Z. Hasan and C. L. Kane, Rev. Mod. Phys. **82**, 3045 (2010).
[13] X.-L. Qi and S.-C. Zhang, Rev. Mod. Phys. **83**, 1057 (2011).
[14] J. L. Zhang, S. J. Zhang, H. M. Weng, W. Zhang, L. X. Yang, Q. Q. Liu, S. M. Feng, X. C. Wang, R. C. Yu, L. Z. Cao, L. Wang, W. G. Yang, H. Z. Liu, W. Y. Zhao, S. C. Zhang, X. Dai, Z. Fang, and C. Q. Jin, Proc. Natl. Acad. Sci. USA **108**, 24 (2011).
[15] K. Matano, M. Kriener, K. Segawa, Y. Ando, and G.-Q. Zheng, Nat. Phys. **12**, 852 (2016).
[16] G. Xu, B. Lian, P. Tang, X. L. Qi, and S. C. Zhang, Phys. Rev. Lett. **117**, 047001 (2016).
[17] Y.-F. Lv, W.-L. Wang, Y.-M. Zhang, H. Ding, W. Li, L. Wang, K. He, C.-L. Song, X.-C. Ma, and Q.-K. Xue, Sci. Bull. **62**, 852 (2017).
[18] Y. Saito, T. Nojima, and Y. Iwasa, Nat. Rev. Mater. **2**, 16094 (2016).
[19] M. Liao, Y. Zang, Z. Guan, H. Li, Y. Gong, K. Zhu, X.-P. Hu, D. Zhang, Y. Xu, Y.-Y. Wang, K. He, X.-C. Ma, S.-C. Zhang, and Q.-K. Xue, Nat. Phys. **14**, 344 (2018).
[20] H. Huang, S. Zhou, and W. Duan, Phys. Rev. B **94**, 121117(R) (2016).
[21] K. Zhang, M. Yan, H. Zhang, H. Huang, M. Arita, Z. Sun, W. Duan, Y. Wu, and S. Zhou, Phys. Rev. B **96**, 125102 (2017).
[22] M. Yan, H. Huang, K. Zhang, E. Wang, W. Yao, K. Deng, G. Wan, H. Zhang, M. Arita, H. Yang, Z. Sun, H. Yao, Y. Wu, S. Fan, W. Duan, and S. Zhou, Nat. Commun. **8**, 257 (2017).
[23] R. C. Xiao, P. L. Gong, Q. S. Wu, W. J. Lu, M. J. Wei, J. Y. Li, H. Y. Lv, X. Luo, P. Tong, X. B. Zhu, and Y. P. Sun, Phys. Rev. B **96**, 075101 (2017).
[24] H. J. Noh, J. Jeong, E. J. Cho, K. Kim, B. I. Min, and B. G. Park, Phys. Rev. Lett. **119**, 016401 (2017).
[25] F. Fei, X. Bo, R. Wang, B. Wu, J. Jiang, D. Fu, M. Gao, H. Zheng, Y. Chen, X. Wang, H. Bu, F. Song, X. Wan, B. Wang, and G. Wang, Phys. Rev. B **96**, 041201 (2017).
[26] M. S. Bahramy, O. J. Clark, B. J. Yang, J. Feng, L. Bawden, J. M. Riley, I. Markovic, F. Mazzola, V. Sunko, D. Biswas, S. P. Cooil, M. Jorge, J. W. Wells, M. Leandersson, T. Balasubramanian, J. Fujii, I. Vobornik, J. E. Rault, T. K. Kim, M. Hoesch *et al.*, Nat. Mater. **17**, 21 (2018).
[27] J. Guggenheim, F. Hulliger, and J. H. Muller, Helv. Phys. Acta **34**, 408 (1961).
[28] H. Leng, C. Paulsen, Y. K. Huang, and A. de Visser, Phys. Rev. B **96**, 220506 (2017).
[29] S. Das, Amit, A. Sirohi, L. Yadav, S. Gayen, Y. Singh, and G. Sheet, Phys. Rev. B **97**, 014523 (2018).
[30] Amit and Y. Singh, Phys. Rev. B **97**, 054515 (2018).
[31] O. J. Clark, M. J. Neat, K. Okawa, L. Bawden, I. Marković, F. Mazzola, J. Feng, V. Sunko, J. M. Riley, W. Meevasana, J. Fujii, I. Vobornik, T. K. Kim, M. Hoesch, T. Sasagawa, P. Wahl, M. S. Bahramy, and P. D. C. King, Phys. Rev. Lett. **120**, 156401 (2018).
[32] G. Kresse and J. Furthmuller, Phys. Rev. B **54**, 11169 (1996).
[33] P. E. Blöchl, Phys. Rev. B **50**, 17953 (1994).
[34] J. P. Perdew, K. Burke, and M. Ernzerhof, Phys. Rev. Lett. **77**, 3865 (1996).
[35] A. V. Krukau, O. A. Vydrov, A. F. Izmaylov, and G. E. Scuseria, J. Chem. Phys. **125**, 224106 (2006).
[36] H. J. Monkhorst and J. D. Pack, Phys. Rev. B **13**, 5188 (1976).
[37] A. A. Mostofi, J. R. Yates, Y.-S. Lee, I. Souza, D. Vanderbilt, and N. Marzari, Comput. Phys. Commun. **178**, 685 (2008).
[38] D. Gresch, G. Autès, O. V. Yazyev, M. Troyer, D. Vanderbilt, B. A. Bernevig, and A. A. Soluyanov, Phys. Rev. B **95**, 075146 (2017).
[39] S. Baroni, S. d. Gironcoli, A. D. Corso, and P. Giannozzi, Rev. Mod. Phys. **73**, 515 (2001).
[40] P. Giannozzi, S. Baroni, N. Bonini, M. Calandra, R. Car, C. Cavazzoni, D. Ceresoli, G. L. Chiarotti, M. Cococcioni, I. Dabo, A. Dal Corso, S. de Gironcoli, S. Fabris, G. Fratesi, R. Gebauer, U. Gerstmann, C. Gougoussis, A. Kokalj, M. Lazzeri, L. Martin-Samos *et al.*, J. Phys.: Condens. Matter. **21**, 395502 (2009).
[41] P. B. Allen and R. C. Dynes, Phys. Rev. B **12**, 905 (1975).
[42] S. Furuseth, K. Selte, and A. Kjekshus, Acta Chem. Scand. **19**, 257 (1965).
[43] D. Zhang, J. Ha, H. Baek, Y. H. Chan, F. D. Natterer, A. F. Myers, J. D. Schumacher, W. G. Cullen, A. V. Davydov, and Y. Kuk, Phys. Rev. Mater. **1**, 024005 (2017).
[44] J. Simonin, Phys. Rev. B **33**, 7830 (1986).
[45] Y. Liu, J.-Z. Zhao, L. Yu, C.-T. Lin, C. Hu, D.-F. Liu, Y.-Y. Peng, Z.-J. Xie, J.-F. He, C.-Y. Chen, Y. Feng, H.-M. Yi, X. Liu, L. Zhao, S.-L. He, G.-D. Liu, X.-L. Dong, J. Zhang, C.-T. Chen, Z.-Y. Xu *et al.*, Chin. Phys. B **24**, 067401 (2015).
[46] F. R. Gamble, J. H. Osiecki, and F. J. DiSalvo, J. Chem. Phys. **55**, 3525 (1971).
[47] See Supplemental Material at http://link.aps.org/supplemental/10.1103/PhysRevMaterials.2.094001 for method of data fitting and more transport, calculation, and spectroscopy data.
[48] Y. Kozuka, M. Kim, C. Bell, B. G. Kim, Y. Hikita, and H. Y. Hwang, Nature (London) **462**, 487 (2009).
[49] A. Gurevich, Physica C **456**, 160 (2007).
[50] A. B. Pippard, Physica **19**, 765 (1953).
[51] J. M. Kosterlitz, Rep. Prog. Phys. **79**, 026001 (2016).
[52] E. F. Talantsev, W. P. Crump, J. O. Island, Y. Xing, Y. Sun, J. Wang, and J. L. Tallon, 2D Mater. **4**, 025072 (2017).
[53] G.-F. Zhang, Y. Li, and C. Wu, Phys. Rev. B **90**, 075114 (2014).
[54] W. L. McMillan, Phys. Rev. **167**, 331 (1968).
[55] Y. Xu, B. Yan, H. J. Zhang, J. Wang, G. Xu, P. Tang, W. Duan, and S. C. Zhang, Phys. Rev. Lett. **111**, 136804 (2013).
[56] A. Molle, J. Goldberger, M. Houssa, Y. Xu, S. C. Zhang, and D. Akinwande, Nat. Mater. **16**, 163 (2017).
[57] X. Xi, L. Zhao, Z. Wang, H. Berger, L. Forro, J. Shan, and K. F. Mak, Nat. Nanotechnol. **10**, 765 (2015).